

## A single-atom detector integrated on an atom chip: fabrication, characterization and application

This article has been downloaded from IOPscience. Please scroll down to see the full text article.

2010 New J. Phys. 12 095005

(<http://iopscience.iop.org/1367-2630/12/9/095005>)

View [the table of contents for this issue](#), or go to the [journal homepage](#) for more

Download details:

IP Address: 128.131.38.115

The article was downloaded on 05/01/2011 at 15:38

Please note that [terms and conditions apply](#).

## A single-atom detector integrated on an atom chip: fabrication, characterization and application

D Heine<sup>1,2</sup>, W Rohringer<sup>1</sup>, D Fischer<sup>1</sup>, M Wilzbach<sup>1,2</sup>, T Raub<sup>1</sup>,  
S Loziczky<sup>1</sup>, XiYuan Liu<sup>3</sup>, S Groth<sup>2</sup>, B Hessmo<sup>1,2</sup> and  
J Schmiedmayer<sup>1,2,4</sup>

<sup>1</sup> Atominstitut, Technische Universität Wien, Stadionallee 2, 1020 Wien, Austria

<sup>2</sup> Physikalisches Institut, Universität Heidelberg, Philosophenweg 12,  
69120 Heidelberg, Germany

<sup>3</sup> Lehrstuhl für Optoelektronik, Universität Mannheim, 68131 Mannheim,  
Germany

E-mail: [schmiedmayer@atomchip.org](mailto:schmiedmayer@atomchip.org)

*New Journal of Physics* **12** (2010) 095005 (23pp)

Received 6 February 2010

Published 9 September 2010

Online at <http://www.njp.org/>

doi:10.1088/1367-2630/12/9/095005

**Abstract.** We describe a robust and reliable fluorescence detector for single atoms that is fully integrated on an atom chip. The detector allows spectrally and spatially selective detection of atoms, reaching a single-atom detection efficiency of 66%. It consists of a tapered lensed single-mode fiber for precise delivery of excitation light and a multi-mode fiber to collect the fluorescence. The fibers are mounted in lithographically defined holding structures on the atom chip. Neutral <sup>87</sup>Rb atoms propagating freely in a magnetic guide are detected and the noise of their fluorescence emission is analyzed. The variance of the photon distribution allows us to determine the number of detected photons per atom and from there the atom detection efficiency. The second-order intensity correlation function of the fluorescence shows near-perfect photon anti-bunching and signs of damped Rabi oscillations. With simple improvements, one can increase the detection efficiency to 95%.

<sup>4</sup> Author to whom any correspondence should be addressed.

**Contents**

<b>1. Introduction</b>	<b>2</b>
<b>2. Basic design</b>	<b>3</b>
<b>3. Implementation</b>	<b>4</b>
3.1. Fabrication . . . . .	5
3.2. Integration in the experiment . . . . .	5
3.3. Excitation of the atoms . . . . .	6
3.4. Light collection . . . . .	7
3.5. Experimental cycle . . . . .	7
<b>4. Characterization of the atom detector</b>	<b>8</b>
4.1. Background . . . . .	8
4.2. Signal strength . . . . .	10
4.3. Photon statistics . . . . .	10
4.4. Single-atom detection efficiency . . . . .	12
4.5. State selectivity . . . . .	13
<b>5. Measurements</b>	<b>14</b>
5.1. Spectroscopy in the magnetic guide . . . . .	14
5.2. Atom cloud extension in the guide . . . . .	15
5.3. Time interval analysis (TIA) . . . . .	16
5.4. Photon antibunching . . . . .	17
<b>6. Future improvements</b>	<b>20</b>
<b>7. Conclusion</b>	<b>21</b>
<b>Acknowledgments</b>	<b>21</b>
<b>References</b>	<b>21</b>

**1. Introduction**

Detecting the state of single neutral atoms selectively is one of the essential ingredients for developing quantum atom optics and atomic physics based quantum technologies and is a prerequisite for many quantum information experiments.

The first single-atom experiments relied on photo ionization for detection [1]. Single-atom observation is now usually performed optically using fluorescence or absorption detection. Cavity-assisted detection schemes are very successful both for absorption detection [2]–[11] and for fluorescence detection [9, 10, 12], but require active stabilization, increasing the complexity and sensitivity to environmental disturbances.

Fluorescence detection of single atoms can be very efficient if the atom remains localized, since long integration times permit the collection of many fluorescence photons. This is realized for single ions in ion traps [13]–[17], for single neutral atoms held in a magneto-optic trap [18]–[21], in dipole traps [22]–[27] and recently in optical lattices [27]–[30]. Fluorescence detection of moving atoms that have a short, finite interaction time with the detector is significantly harder and requires both supreme background suppression and high collection efficiency to reach single-atom sensitivity [31]–[33].

A powerful tool for experiment with ultracold neutral atoms is atom chips [34], which employ micro-fabricated wires and electrodes to generate magnetic and electric fields for quantum manipulation of neutral atoms a few micrometers above the chip surface [35]–[37]. Many components of integrated matter wave technology have been demonstrated, including combined magnetic/electrostatic traps [38], motors and shift registers [39], atomic beam splitters [40], the creation of Bose–Einstein condensation (BEC) [41]–[43], atom interference [44, 45] and the integration of optical lattices [46].

Recently, it was demonstrated that atoms in magnetic guides [47] or on chips can be detected by field ionization near nano-structures [48, 49], by mounted optical fibers in absorption [50], in fluorescence [51], by using integrated waveguides [52] or with the help of cavities [8, 9, 11]. The latter require active alignment and are technologically very challenging. Miniaturizing the different highly sophisticated and efficient optics detection methods benefits from scaling with size [53] and allows integration.

In this paper, we describe in detail the design, implementation and application of our very simple and robust integrated *fluorescence* detector [51] that reaches a single-atom detection efficiency of  $\eta_{\text{at}} = 66\%$  and a high signal-to-noise ratio (SNR) of up to 100 without the need either for localization of the atoms in a trap or the assistance of a cavity. The miniaturized detector is based on optical fibers fully integrated on an atom chip [54, 55] using lithographically fabricated SU-8 mounting structures [56] and allows us to examine the statistical distribution of the atoms in a magnetic guide, and to observe the non-classical fluorescence emission of single atoms [57]. In the outlook, we discuss a straightforward improvement to our present setup that will allow us to build atom counters with close-to-unity efficiency fully integrated on the atom chip.

## 2. Basic design

A very simple way of detecting an atom is by observing its fluorescence. The basic idea is to drive a (closed) transition of the atom to an excited state with an external light field and to detect the spontaneously emitted photons. The sensitivity of the detection and its fidelity depend on the number of scattered photons, the detection efficiency of the scattered light and the suppression of background noise. A well-designed fluorescence detector collects as much light as possible and simultaneously has a negligible background. In the ideal case, a single detected photon implies that an atom is present in the detection region.

In principle, there is no fundamental limit to the efficiency of a fluorescence detector as long as the atom is not lost from the observation region. Long integration times allow the collection of many fluorescence photons and efficient discrimination from the background. Such a setting has been realized for single ions in ion traps [13]–[17], for a single neutral atom in a dipole trap [22]–[27] or for counting neutral atoms in a magneto-optical trap [18]–[21]. Free neutral atoms are considerably harder to detect, because the few scattered photons are difficult to distinguish from the background light.

We achieve efficient light collection with small background by employing a fiber optical setup [51], as shown in figure 1(a). Our fluorescence detector is built using a single mode tapered lensed fiber, which delivers the excitation light, and a multi-mode fiber to collect the fluorescence. The multi-mode fiber is aligned at  $90^\circ$  to the tapered lensed fiber. The excitation of the atoms is at the very small focal spot of the lensed fiber. The collection fiber collects light preferably from the region around that focal spot. Altogether, such an arrangement leads to efficient light collection and superb reduction of background. If no atom is present in the beam

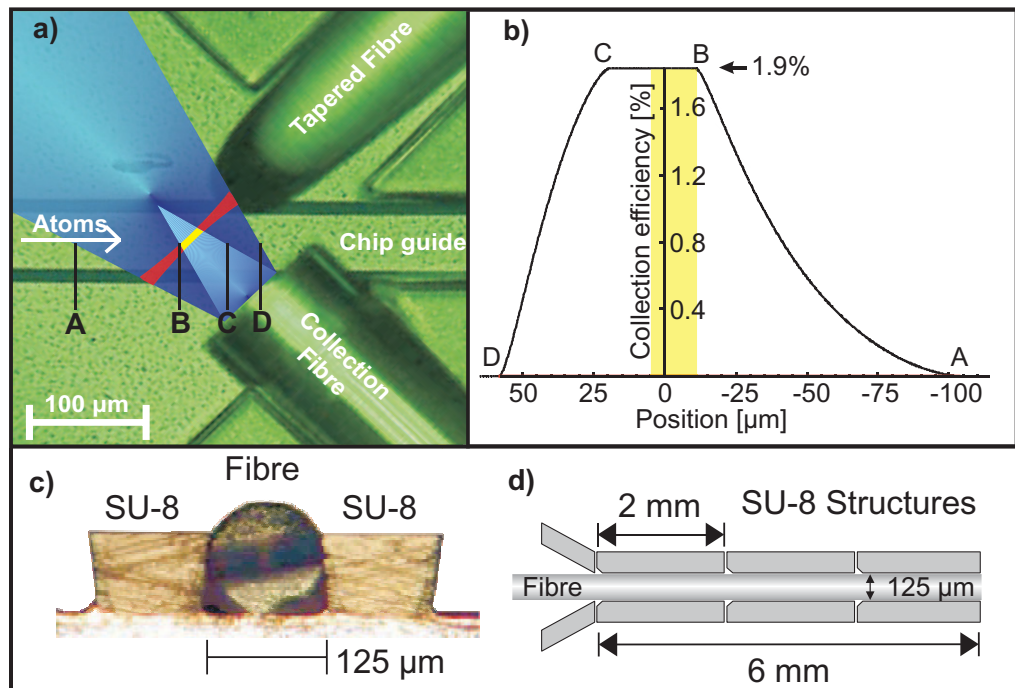


**Figure 1.** Details of the integrated atom detector. (a) The multi-mode fiber preferentially collects light from a cone (light blue) determined by its NA. The overlap of this cone with the excitation light (red) from the tapered fiber defines the detection region (yellow). (b) Calculated collection efficiency of the multi-mode fiber for different longitudinal positions along the guide wire. The yellow overlay indicates the region where atoms interact with the excitation light. (c) Image showing a cross-section illustrating the mounting of the optical fibers by the undercut SU-8 structure that clamps the fiber to the chip surface. (d) Schematic view of the lithographically defined SU-8 holding structure. The total length of 6 mm ensures excellent pointing stability, while segmentation into 2 mm long sections allows for thermal expansion of the underlying chip. To ease insertion of the fibers during construction a funnel has been included in the design.

focus, very little light is scattered into the fiber. As soon as an atom is present, the multi-mode fiber collects scattered photons from the atom.

### 3. Implementation

For stable and reliable operation, both the excitation and detection fibers should be fully integrated into the atom chip. External mountings are poor alternatives, since they might move relative to the chip structures and hence lead to non-reproducible results. The fibers can be glued to the chip by first employing fiber grippers for positioning and alignment. While this method may result in good alignment, it is cumbersome to employ and requires significant time and skill to achieve consistent results. Lithographically fabricated robust and precise fiber mounting structures [56] are a great help in assembling the detector.

### 3.1. Fabrication

Our atom chip holding the microstructures and the detector are fabricated on a  $700\ \mu\text{m}$  thick silicon substrate. Using optical lithography, the microstructures to manipulate the atoms are patterned into a high-quality evaporated gold layer [54, 55] of  $2\ \mu\text{m}$  thickness. These wire microstructures support current densities exceeding  $2 \times 10^7\ \text{A cm}^{-2}$  without the risk of wire destruction.

To achieve the precise alignment of the fibers and robust integration on the atom chip, we employ a lithographically patterned layer of SU-8 on top of the chip structures. SU-8 [58] is an epoxy-based negative photoresist that is typically developed using UV-radiation in the range 365–436 nm. SU-8 has high mechanical, chemical and thermal stability. Its specific properties facilitate the production of thick structures with very smooth, nearly vertical sidewalls. With a single SU-8 layer, a coating film thickness of up to  $300\ \mu\text{m}$  is possible. Once fully developed, its glass transition temperature is approximately  $200\ ^\circ\text{C}$ , with a degradation threshold of around  $380\ ^\circ\text{C}$ . Neither of these temperatures is reached during the operation of the atom chip.

The fibers are held in  $90\ \mu\text{m}$  deep and  $125\ \mu\text{m}$  wide SU-8 trenches, corresponding to the fiber diameter. Careful selection of the fabrication parameters produces slightly undercut sidewalls, as shown in figure 1(c). The layer thickness of  $90\ \mu\text{m}$  is chosen to be larger than the fiber radius, which allows the undercut to effectively clamp the fibers to the chip surface. The total length of the trenches was chosen to be 6 mm, sectioned into three 2 mm long substructures to reduce mechanical stress during thermal expansion (figures 1(c) and (d)). The entry port is funneled to simplify the insertion of the fiber.

In fabricating the fiber mounts, a 7.5% shrinkage of the SU-8 during development has to be taken into account [58], leading to a slight variability in the dimensions of the holding structures. It should be noted here that the variations in fiber diameters are large in comparison. The diameter of a fiber used in the experiment is specified with a precision of only  $1\ \mu\text{m}$  to a cladding diameter of  $125 \pm 1\ \mu\text{m}$ . Therefore, we fabricated a set of three parallel mounting structures with slightly different sizes ( $124.5$ ,  $125$  and  $125.5\ \mu\text{m}$ ).

To assess the quality and stability of the alignment structures and the glued fibers, we used the SU-8 structures to hold fiber optical resonators with a  $\sim 5\ \mu\text{m}$  gap [59]. The finesse of the resonator strongly depends on losses introduced by misalignment at the gap. In our tests, we measured a very small additional average loss in the spliced and mounted resonators of  $\sim 0.3\%$ , which, neglecting other additional losses, corresponds to a maximal transversal misalignment of less than 100 nm, while angular misalignment is negligible because of the long insertion funnels. In the test experiments, the alignment precision of the SU-8 structures was superior to the precision that can be achieved using a combination of fiber-grippers and piezo-drive nano-position stages. Longitudinal alignment precision for the fiber cavity is better than 500 nm. Cycling the temperature up to  $100\ ^\circ\text{C}$  and back resulted in no measurable misalignment of the fibers.

The long-term stability is excellent. We could observe no degradation in our fluorescence detector for more than 3 years under the experimental conditions, including a move of the whole experiment from Heidelberg to Vienna.

### 3.2. Integration in the experiment

Given the diameter of the mounted fibers of  $125\ \mu\text{m}$ , the detection region is situated  $62.5\ \mu\text{m}$  above the chip surface. To avoid stray light from the mounting structures when loading the

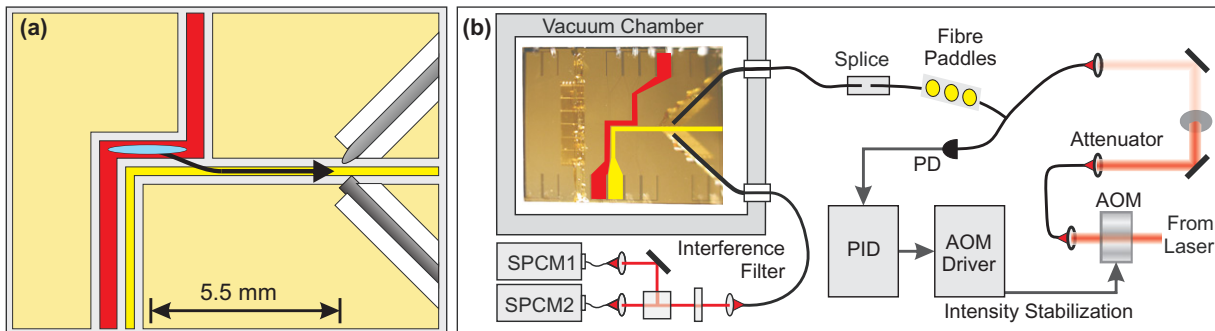


**Figure 2.** Details of the atom chip setup and detector. (a) Schematic layout of the atom chip. Atoms are initially trapped in a magnetic trap generated by a Z-shaped wire (red). A magnetic guide (yellow) transports the atoms to the focus of the tapered lensed fiber. (b) Basic layout of the detector experiment and the atom chip. Light from a frequency-stabilized source is delivered via a tapered lensed fiber to the interaction region. Part of the light is split off in a commercial fiber beam splitter and directed to a PIN-type PD for intensity stabilization (PID) using an acousto-optical modulator (AOM), which can also be used as a fast light switch. The polarization of the excitation light is adjusted using mechanical fiber paddles, optimizing for maximal fluorescence signal. The light scattered by the atoms is collected by a multi-mode fiber that guides the light to one single photon counting module (SPCM) for high-efficiency atom detection or two SPCMs in Hanbury Brown and Twiss configuration for correlation measurements.

atoms in the mirror MOT, the detector is built 5.5 mm away from the chip center. A magnetic guide on the chip delivers the atoms to the detector (see figure 2).

The fibers mounted on the atom chip are then connected to the outside of the vacuum chamber via an ultra-high vacuum (UHV) compatible feed-through [60]. The whole setup can be baked to 100 °C and achieves UHV below  $10^{-10}$  mbar.

### 3.3. Excitation of the atoms

To excite the atoms, the tapered lensed fiber delivers light to the guide potential minimum. Our tapered fibers have a focal length of  $40 \mu\text{m}$  with a focal diameter of  $5 \mu\text{m}$ . For the  $F = 2 \rightarrow F' = 3$  transition in  $^{87}\text{Rb}$ , saturation intensity is reached in the focus at a power of  $P_{\text{sat}} = 325 \text{ pW}$ . The focus of the tapered fiber defines the interaction region, as shown in figure 1(a), and is located  $62.5 \mu\text{m}$  (half a fiber diameter) above the chip surface.

The excitation light is generated by an external cavity diode laser (ECDL) frequency stabilized to the  $F = 2 \rightarrow F' = 3$  transition with a precision better than 1 MHz, smaller than the natural linewidth of the transition. The probe laser is frequency stabilized to a reference laser by means of a frequency offset (beating) lock. This locking scheme enables us to shift the lock point by several hundreds of MHz during operation, allowing us to probe the atomic ensemble over the full range of the Rb–D2 transition.

For additional intensity stabilization, part of the light is split off into a commercial fiber beam splitter and directed to a PIN-type photo diode (PD) (see figure 2(b)). The PD signal

is fed into custom-built proportional–integral–differential lock electronics (PID) stabilizing the beam power with an uncertainty below 10 pW for total powers between 300 pW and several nW to the set value by controlling the output level of an AOM used to regulate the intensity. The polarization of the excitation light can be rotated by employing mechanical fiber paddles. It was adjusted for maximal light output of the atom detector. The long-term stability of the polarization can be estimated by the intensity drop of the collected light. Typical intervals between realigning the polarization was days. Fast fluctuations were not observed.

Using a mechanical fiber splice, the stabilized excitation light is coupled into the single-mode tapered lensed fiber guiding the light into the vacuum chamber to the detection region.

### 3.4. Light collection

Light scattered by the atoms is collected by a multi-mode fiber that guides the light to an SPCM. To protect the SPCM and to filter non-resonant background light, a narrow interference filter is included in the beam path (3 nm FWHM).

The multi-mode fiber has a limited field of view, given by its numerical aperture of  $NA = 0.275 \pm 0.015$  and the core diameter of  $62.5 \pm 1 \mu\text{m}$ . Only light hitting the core at angles up to maximally  $\arcsin(NA) = 16^\circ \pm 0.9^\circ$  will be collected. Consequently, only the emission from atoms within the light-blue cone marked in figure 1(a) is collected with the full NA, while collection efficiency rapidly drops outside this region, within the dark-blue cone, as suggested by calculations depicted in figure 1(b).

The height of the detection region is automatically aligned to the excitation region, since the outer diameters of the fibers match. By aligning the MM fiber such that the collection cone defined by the numerical aperture overlaps with the excitation region, we reach both a highly selective excitation of the atoms and a matched collection region. The angle between the tapered (excitation) and the multi-mode (detection) fiber was chosen to be  $90^\circ$ . This leads to an excellent geometrical suppression of stray light. Of each nW of excitation light only about 30 photons per second are collected by the detection fiber, corresponding to a stray light suppression better than  $10^{-8}$ . The detection setup has been positioned such that both fibers are at  $45^\circ$  to the guide to avoid the blocking of the guide.

For the given NA, a maximum photon collection efficiency of  $\eta_{\text{coll}} = 1.9\%$  can be determined. Together with the finite efficiency  $\eta_{\text{SPCM}} = 0.56$  of the SPCM and optical losses, this leads to a total photon detection efficiency of  $\eta_{\text{ph}} = 0.9\%$ .

### 3.5. Experimental cycle

In our experiments, the atom chip [34, 35] serves as the experimental platform for efficient cooling and trapping of the atoms and for their delivery to the detection region in a magnetic guide.

Our experimental procedure is described in [61]. The heart of our setup is a hybrid macroscopic–microscopic atom chip assembly. It holds the macroscopic wire structures used to pre-cool and capture the atoms in the primary phase of the experiment, as well as the appropriately designed wire microstructures on the atom chip needed for trapping and manipulating the atoms, including the atom detector.

The experimental procedure typically starts with more than  $10^8$   $^{87}\text{Rb}$  atoms accumulated in a mirror MOT. The atoms are subsequently optically pumped into the  $|F = 2, m_F = 2\rangle$  state and transferred to a Ioffe–Pritchard-type magnetic trap on the atom chip generated by a Z-shaped wire on the chip surface. The procedure is optimized by a genetic algorithm [62]. The atoms in the magnetic trap are released into a magnetic guide (L-shaped wire), where the atomic cloud can expand toward the detector. The position of the magnetic guide above the chip surface is aligned with the focus of the tapered lensed fiber at the detection region by adjusting the current through the chip wire (vertical alignment) and the strength and orientation of the external magnetic field (vertical and horizontal alignment). See [35] for details.

When the atoms are released from the initial Z trap into the magnetic guide, they thermally expand toward the detector. In the focus of the lensed fiber, the atoms are excited by a laser operating near one of the rubidium D2 transitions, for example tuned to the  $F = 2$  to  $F' = 3$  transition. The fluorescence photons are then collected by the multi-mode fiber and detected by an SPCM, their arrival times are recorded with 1 ns resolution. The experiment is repeated several times to measure the photon statistics. A typical signal is shown in figure 3(a).

In the current experiment, the phase space density in the magnetic trap and guide is always less than  $10^{-5}$ .

#### 4. Characterization of the atom detector

One observation in our experiments is that we see the full length of the atom pulse guided in the magnetic guide (figure 3(a)), even though the resonant excitation light of the detector is always on. These measurements show that in our experiments the effects of stray excitation light on the guided atoms can be neglected. This is quite remarkable, since magnetic traps are extremely sensitive to light scattering. On average, scattering of a little more than a single photon is sufficient to pump the atom into a magnetically untrapped state, removing it from the magnetic guide.

Figure 3(a) shows the atomic signal together with its variance, calculated from 600 consecutive measurements. The shape can be described by a one-dimensional (1D) Maxwell–Boltzmann distribution given by the temperature of the atoms when the reflection of the part of the atom cloud that starts to expand toward the closed end of the guide is also taken into account. The measured temperature of  $25\ \mu\text{K}$  agrees with independent measurements via time-of-flight methods.

##### 4.1. Background

The fiber-based detector presented here has an exceptionally low background count rate of only  $\sim 300$  counts per second (cps) at 1 nW resonant probe light. The dominating contribution is the dark counts ( $\sim 260$  cps) of the employed photon counter (Perkin-Elmer, SPCM-AQR-12).

Despite the proximity of the atom chip surface (at a distance of  $62.5\ \mu\text{m}$ ), the influence of stray probe light is essentially eliminated with a suppression better than  $10^{-8}$ . 1 nW excitation light contributes only  $\sim 30$  cps to the background.

This excellent suppression of stray light is achieved by the fact that a tapered lensed fiber delivers excitation light efficiently to a very small detection region and the multi-mode fiber, mounted at an angle of  $90^\circ$ , selectively collects the fluorescent photons from this small volume (figure 1(a)). Basically, all the background light originating from scattering on the nearby chip

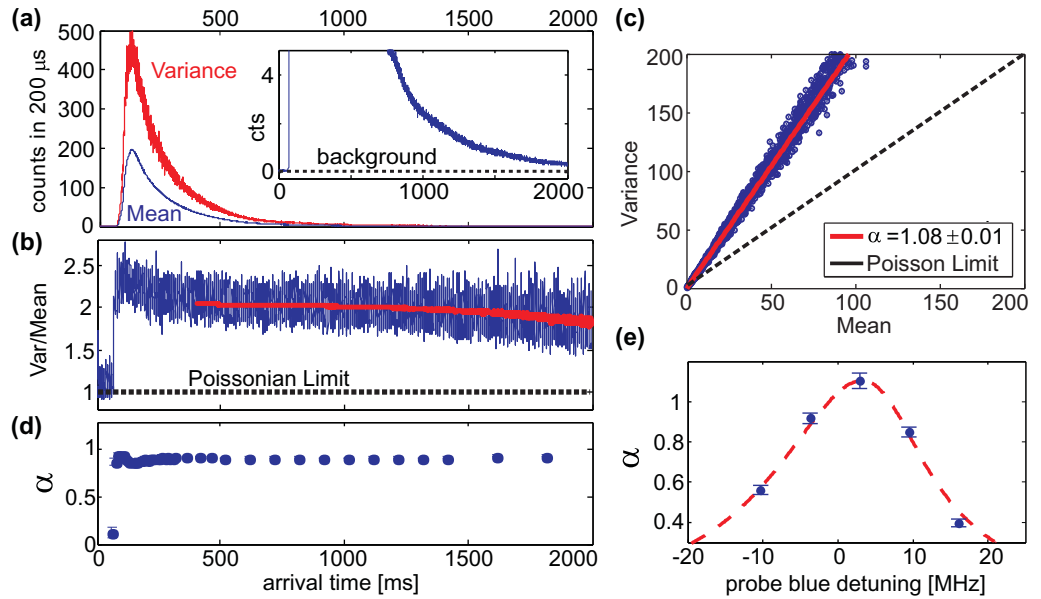


**Figure 3.** Photon count signal from the atom detector. (a) Mean and variance of the photon counts: the lower (blue) curve shows the mean photon count  $\langle n \rangle$  for 600 experimental runs, whereas the upper (red) curve shows their variance  $\text{Var}(n)$ . An integration time of  $t_{\text{int}} = 200 \mu\text{s}$  has been used. Inset: even after 2 s the signal is still significantly above the background level of 0.06. (b) Ratio  $\text{Var}(n)/\langle n \rangle$ : as soon as the atoms arrive,  $\text{Var}(n)/\langle n \rangle$  exhibits a sudden jump to a super-Poissonian value of  $1 + \alpha$ . Even though  $\alpha$  remains constant, the ratio decreases with atomic density as background becomes more important. The red line gives a fit according to equation (2) (including the background) over more than two orders of magnitude in atom density. Note that the initial overshoot is an artifact of the analysis, because around the peak the steep slopes cannot be neglected during the  $200 \mu\text{s}$  integration time. (c)  $\text{Var}(n)$  as a function of the mean recorded count rate  $\langle n \rangle$ . An analysis according to equation (2) (red line) yields a signal strength of  $\alpha = 1.08 \pm 0.01$  counts per atom (integration time  $t_{\text{int}} = 300 \mu\text{s}$ ). The dashed line corresponds to Poissonian statistics. (d) The signal strength  $\alpha$  remains constant and is independent of atom density over three orders of magnitude. Here,  $\alpha$  is evaluated for a shorter  $t_{\text{int}} = 50 \mu\text{s}$  and shows a reduced value of  $\alpha = 0.94$  (compare figure 4). (e)  $\alpha$  as a function of the probe beam detuning reveals an optimal blue detuning of 3 MHz. The dashed red line is a model based on [32].

surface or the vacuum chamber is blocked very efficiently, because it is not matched to the guided modes in the collection fiber.

Other background sources are stray light from the outside and the glow of the hot dispensers. An interference filter efficiently suppresses this remaining background to below 10 cps (see figure 2(b)).

The excellent stray light suppression and overall small background level allow high-fidelity detection of a single atom and accurate measurements of photon and atom statistics.

#### 4.2. Signal strength

An important parameter of the detector is the total number of photons that can be scattered by atoms passing the detection region before they are lost for the detection process. We discuss this here for detecting  $^{87}\text{Rb}$  atoms in  $F = 2$  using the  $F = 2 \rightarrow F' = 3$  transition. The total number of scattered photons can be estimated from the ratio of the fluorescence counts when exciting on the closed  $F = 2 \rightarrow F' = 3$  transition to the fluorescence counts on the open transition  $F = 2 \rightarrow F' = 1$ . Exciting on the latter, an atom scatters slightly more than one photon before being optically pumped into the other hyperfine ground state, where it remains dark. We find that in our detector each atom scatters  $\sim 120$  photons when excited on the  $F = 2 \rightarrow F' = 3$  transition. The limit of 120 scattered photons comes from a combination of different effects. (a) Atoms are accelerated by the excitation light and can be pushed out of the interaction region. (b) Atoms leave the guide and are pushed into regions of larger magnetic field, which leads to a detuning from the excitation light. (c) Atoms are optically pumped into different magnetic states, which will have larger detuning.

Combining this number with the overall photon detection efficiency  $p_{\text{det}} = 0.9\%$  given above, we estimate that our detector sees on average  $\alpha \sim 1.1$  photons from each atom passing by. This number was confirmed with independent global atom number measurements using absorption imaging.

The maximum signal per atom is generated not for resonant illumination, as might be expected, but for a blue detuning of 3 MHz of the exciting light field, as shown in figure 3(e). Looking more into the details, the atoms accumulate a time-dependent detuning  $\delta(t)$  during interaction with the probe field due to photon recoil-induced Doppler shift. An initial blue detuning pushes the atoms through resonance to maximize the total number of scattered photons during the interaction time [32].

#### 4.3. Photon statistics

When an atom arrives at the detector, it absorbs and then re-emits photons. A few of these photons are counted by the SPCM. This photon scattering strongly disturbs the atom. In addition to the photon recoil, scattering will pump the atom into an untrapped state and eventually into a different hyperfine ground state that is not excited by the probing light. Consequently, after some time the atom will either leave the detection region and/or stop scattering photons. During detection, each atom emits a photon burst, and on average  $\alpha$  photons are detected per atom. These photon bursts lead to a super-Poissonian statistics for the detected photons (figure 3(b)). As we will show below, we can relate the variance and the mean of the photon counts directly to the average number of photons detected per atom ( $\alpha$ ).

A coherent light source of constant mean photon number  $\langle n \rangle$  creates a Poisson-distributed photon stream with variance equal to the mean,  $\text{Var}(n) = \langle n \rangle$ , and hence

$$\left. \frac{\text{Var}(n)}{\langle n \rangle} \right|_{\text{Poisson}} = 1.$$

The super-Poissonian photon statistics for the atom detection events can be seen in figure 3(b) by the jump of  $\text{Var}(n)/\langle n \rangle > 1$  as soon as atoms reach the detector. The statistical atom number fluctuations lead to an increase in the photon noise. The atom number follows its own statistical distribution  $p(m)$  around a mean value  $\langle m \rangle$ , and Mandel's formula [63] can be used to describe

the photon count distribution in the presence of atoms. The probability  $p(n)$  to measure  $n$  counts is then expressed by folding the conditional probability

$$p(n)|_m = \frac{(m \cdot \alpha)^n}{n!} e^{-m \cdot \alpha}$$

to measure  $n$  counts in the presence of  $m$  atoms with the atom number probability distribution  $p(m, \langle m \rangle)$ .

$$p(n) = \sum_{m=0}^{\infty} p(m, \langle m \rangle) \cdot p(n)|_m.$$

The ratio  $\text{Var}(n)/\langle n \rangle$  can then be calculated to

$$\frac{\text{Var}(n)}{\langle n \rangle} = 1 + \alpha \frac{\text{Var}(m)}{\langle m \rangle}. \quad (1)$$

Hence, the ratio of the variance of the photon counts to its mean value deviates from the Poissonian value 1 by the number of photon counts per atom  $\alpha$  times the ratio of variance to mean of the atom number.

If, in addition, a Poissonian background  $bg$  with  $\text{Var}(bg) = bg$  is taken into account equation (1) is modified and the photon statistics can be expressed as

$$\frac{\text{Var}(n)}{\langle n \rangle} = 1 + \alpha \frac{\text{Var}(m)}{\langle m \rangle + \langle bg \rangle / \alpha}. \quad (2)$$

It is worth noting that this relation is independent of the actual atom number. For a Poissonian atom number distribution, i.e.  $\text{Var}(m)/\langle m \rangle = 1$ , the signal strength  $\alpha$  can be measured as the slope of the relation variance versus mean (see figure 3(c)). Conversely, if  $\alpha$  is known, equation (2) makes it possible to examine the statistical distribution of the atoms by measuring the photon count distribution. Figures 3(b) and (c) show the measured ratio  $\text{Var}(n)/\langle n \rangle$  and  $\text{Var}(n)$  versus  $\langle n \rangle$ , together with a fit according to equation (2), respectively. The signal strength is  $\alpha = 1.08 \pm 0.01$  cpa, independent of atomic density over three orders of magnitude, as demonstrated in figure 3(d).

A detailed analysis of the distributions shows that an integration time  $t_{\text{int}} = 300 \mu\text{s}$  is needed to collect the full signal. Specific applications will benefit from shorter integration times. Figure 4 illustrates that  $\alpha$  drops rather slowly when reducing the integration time, while the mean number of background counts  $\langle bg \rangle$  is a linear function of  $t_{\text{int}}$ . For  $t_{\text{int}} = 100 \mu\text{s}$ , the integrated signal is  $\alpha = 1.01$  cpa and even for  $t_{\text{int}} = 50 \mu\text{s}$  we still find  $\alpha = 0.94$  cpa.

To model the atom detection process and the experimental data of figure 4(a), we developed a simple Monte Carlo model. We start with a Poisson-distributed atom flux. From each atom, on average  $\alpha$  photons are detected according to a Poisson distribution. For simplicity, we assume a constant average photon detection rate  $R = 1/\tau$  from each atom in the detector ( $\tau$  is then the mean distance between detected photons in the photon burst). The results of such a model calculation with three different photon detection rates  $R = 1/\tau$  with  $\tau = 5, 7$  and  $10 \mu\text{s}$  are displayed in figure 4(a). Even though the assumption of a constant photon detection rate is a very rough simplification, the model with  $\tau = 7 \mu\text{s}$  describes the data well. We will use this simple model again in section 6 to evaluate possible future improvements of the detector.

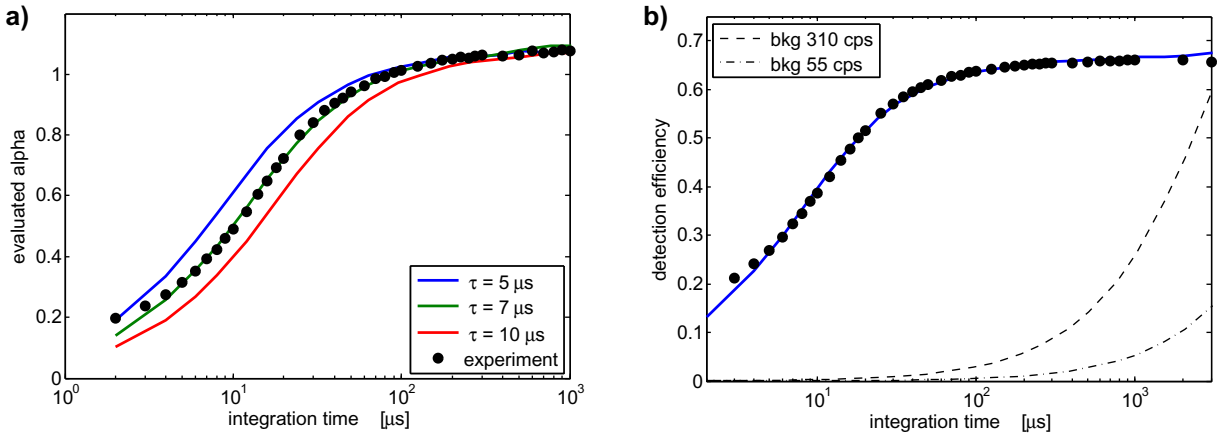


**Figure 4.** (a) Signal strength  $\alpha$  as a function of the integration time  $t_{\text{int}}$ . While  $300 \mu\text{s}$  are needed to collect the full signal,  $\alpha$  drops only slowly for shorter integration times. The measured data are compared to the simple Monte Carlo detection model, with different decay rates for the atomic signal. The model with an average photon detection rate  $R = 1/\tau$  with  $\tau = 7 \mu\text{s}$  gives the best agreement. (b) Single-atom detection efficiency (solid blue line) and false positive detection probabilities (dotted lines) for background rates of 311 and 55 cps versus integration time.

**Table 1.** Single-atom detection efficiency  $\eta_{\text{at}}$  and false detection probability  $p_f$  as a function of the integration time for the current system ( $\text{NA} = 0.275$ ,  $\eta_{\text{ph}} = 0.9\%$ ,  $\langle bg \rangle = 310 \text{ cps}$ ). The SNR is defined as  $\text{SNR} = \alpha(t_{\text{int}})/\langle bg(t_{\text{int}}) \rangle$ . Numbers in parentheses are obtained assuming using a low-noise SPCM ( $\langle bg \rangle = 55 \text{ cps}$ ).

$t_{\text{int}}$	$\alpha$ (cpa)	$\eta_{\text{at}}$	$p_f$	SNR
$300 \mu\text{s}$	1.08	66%	9%	11 (65)
$45 \mu\text{s}$	0.92	60%	1.4%	65 (372)
$20 \mu\text{s}$	0.72	50%	0.6%	116 (655)

#### 4.4. Single-atom detection efficiency

If we must count at least one photon to see an atom, the single-atom detection efficiency is given by

$$\eta_{\text{at}} = 1 - \exp(-\alpha).$$

In our experiment, we find  $\eta_{\text{at}} = 66\%$  for  $300 \mu\text{s}$  integration time. Background counts during this time lead to a false positive detection probability of  $p_f = 9\%$ . The relation between detection efficiency  $\eta_{\text{at}}$  and integration time  $t_{\text{int}}$  is shown in figure 4(b), together with the false positive detection probability for the current setup and a background reduced setup. While the detection efficiency is determined by the finite NA of the collection fiber, the SNR is mainly limited by the background. Exchanging the SPCM by a low-noise model with a dark count rate below 25 cps, a total background as low as 55 cps can be reached.

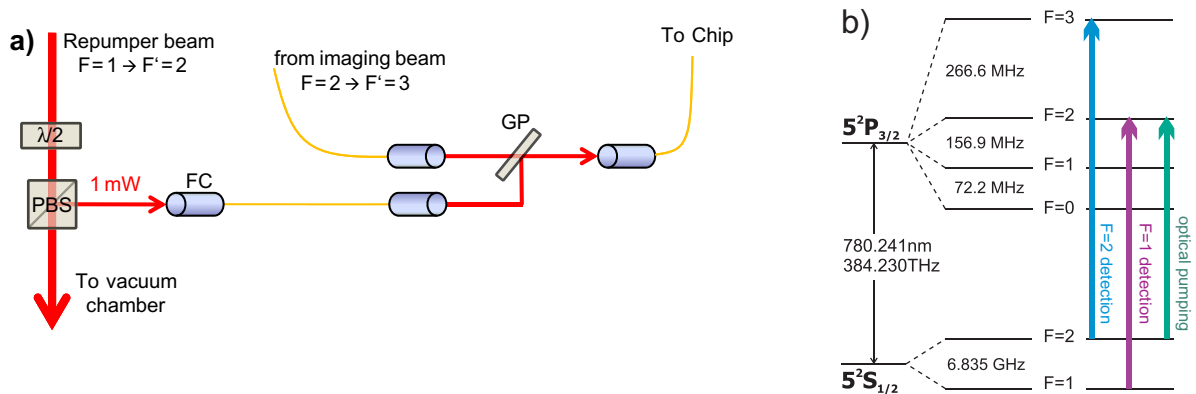


**Figure 5.** Changes in the detector setup for  $F = 1$  detection. (a) Scheme to deliver light to the integrated atom detector for both  $F = 1$  and  $F = 2$  detection. The  $F = 1$  detection light is taken from the repumping beam of the MOT. (b) Level scheme of  $^{87}\text{Rb}$  D2 line with the relevant transitions for  $F = 2$  detection,  $F = 1$  detection and the transition used to prepare the  $F = 1$  sample by optical pumping from the  $F = 2$  to the  $F = 1$  ground state.

At  $t_{\text{int}} = 45 \mu\text{s}$ , the atom detection efficiency is  $\eta_{\text{at}} = 60\%$  with a false detection probability  $p_f$  of only  $p_f = 1.4\%$  (see table 1). Defining  $\text{SNR} = \alpha(t_{\text{int}}) / \langle bg(t_{\text{int}}) \rangle$ ,  $\text{SNR} = 100$  is reached in the current setup at  $t_{\text{int}} = 25 \mu\text{s}$  ( $\eta_{\text{at}} = 55\%$ ). At a background level of 55 cps,  $\text{SNR} = 100$  will already be reached at  $t_{\text{int}} = 175 \mu\text{s}$  ( $\eta_{\text{at}} = 65\%$ ).

#### 4.5. State selectivity

A key signature of an ideal atom detector is the selectivity to internal states; distinguishing between the two hyperfine ground states is most important. Most atoms used in ultracold atom experiments have a sizable hyperfine splitting in the ground state, and consequently the two ground states can very easily be distinguished by (near) resonant fluorescence excitation, and state selectivity comes naturally.

One characteristic of our fluorescence detector is that, for high detection efficiency, many scattered photons per atom are necessary, and consequently one needs to use a closed atomic transition. In our present experiment, we use  $^{87}\text{Rb}$  atoms with the two hyperfine ground states ( $F = 1$  and  $F = 2$  separated by 6.8 GHz). From the  $F = 2$  ground state there is a closed transition ( $F = 2 \rightarrow F' = 3$ ) where one can scatter  $> 1000$  photons before changing the hyperfine ground state by off-resonant excitation.

For atoms in the  $F = 1$  ground state the situation is not so simple. To ensure a high scattering rate, excitation on the  $F = 1 \rightarrow F' = 2$  transition is advantageous. This transition leads to rapid optical pumping into the other hyperfine ground state  $F = 2$ , and light scattering stops. This can be overcome by adding a second excitation laser tuned to the  $F = 2 \rightarrow F' = 3$  transition. With both lasers on, one can also scatter many photons off atoms in the  $F = 1$  hyperfine ground state and detect them. For large powers ( $> 300 \text{ pW}$ ) of light resonant with the  $F = 1 \rightarrow F' = 2$  transition, the signal strength  $\alpha$  has been measured to be comparable to the case of atoms in the  $F = 2$  ground state. The results of our measurements are summarized in table 2.

Introducing the re-pumping laser means that a detector probing  $F = 1$  will also detect  $F = 2$ . For state-selective detection, this is not so much of a problem, because one can arrange

**Table 2.** Signal strength for detecting  $F = 1$  and  $F = 2$  atoms with the  $F = 1$  and  $F = 2$  detection schemes for an integration time of  $300 \mu\text{s}$ . The values correspond to single atom detection efficiencies of 66% for the  $F = 2$  and 64% for the  $F = 1$  states, respectively. In the  $F = 1$  detection scheme, the  $F = 1 \rightarrow F' = 2$  ‘repumper’ light had a power of 300 pW. The slightly lower value for the  $F = 1$  detection scheme can be associated with excess background, due to the additional excitation light. If we turn off the repumper light, atoms in the  $F = 1$  ground state do not create a detection signal at all.

	Detector $F = 1$	Detector $F = 2$
Atoms $F = 1$	1.03	–
Atoms $F = 2$	1.03	1.08

two detectors in such a way that the first detector measures the  $F = 2$  atoms. This detector removes the  $F = 2$  atoms from the guide, but leaves the  $F = 1$  atoms propagating. A second detector behind the  $F = 2$  detector with both excitation frequencies will register the remaining atoms, all in  $F = 1$ .

## 5. Measurements

We have employed our detector in a series of experiments to illustrate its robustness and versatility.

### 5.1. Spectroscopy in the magnetic guide

To demonstrate that the integrated fluorescence detector allows selective addressing of atomic levels, we have measured the signal of an atom pulse passing the detector for different frequencies of the probe light.

For these measurements, the atoms are prepared such that upon arrival at the detector the atoms are in the  $|F = 2, m_F = 2\rangle$  ground state and can be excited to the  $F' = 1, 2$  or 3 state. Figure 6 displays the results of a 600 MHz sweep, starting 60 MHz blue detuned of the  $F' = 3$  transition and going down to more than 100 MHz red detuning of the  $F' = 1$  transition. The transition  $F = 2 \rightarrow F' = 3$  gives the strongest signal, as expected, and has correspondingly been employed for the high-efficiency atom detection presented in the remaining sections of this paper. The  $F = 2 \rightarrow F' = 1$  transition gives the weakest signal, an atom scatters slightly more than one photon before being optically pumped into the other hyperfine ground state, where it remains dark. As discussed above, the ratio between the signals observed for the  $F = 2 \rightarrow F' = X$  and  $F = 2 \rightarrow F' = 1$  transitions can be used to estimate how many photons the atom scatters at the  $F = 2 \rightarrow F' = X$  transition. In an optimized setting, we observe that the  $^{87}\text{Rb}$  atoms scatter about 120 photons on the  $F = 2 \rightarrow F' = 3$  transition before they leave the detector.

For the measurement displayed in figure 6, the remaining magnetic field at the guide minimum of approximately 4 G was chosen. This field leads to a Zeeman splitting of the magnetic sublevels. The splitting between adjacent levels is smaller than the linewidth for

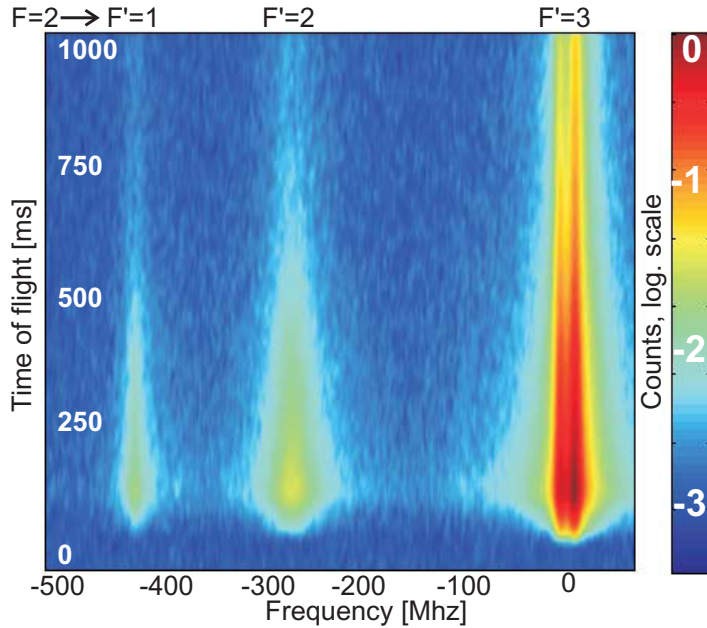


**Figure 6.** Spectroscopy of atoms in the guide by scanning the frequency of the detection light over 600 MHz, displaying the count rate at the detection region. To enhance the clarity of the presentation the graph uses a logarithmic scale in count rate. The scale is given in counts per  $\mu\text{s}$ . Transitions from the  $F = 2$  ground state to  $F' = 1, 2, 3$  excited states are resolved. Note that in the  $F' = 3$  transition, the two cyclic transitions  $m_F = 2 \rightarrow m'_F = 3$  and  $m_F = -2 \rightarrow m'_F = -3$  can be distinguished due to Zeeman splitting induced by the magnetic guiding field minimum, which was chosen to be at 4 G for this measurement.

the  $F' = 1$  and  $F' = 2$  transitions; hence, only one peak is observed. Note, however, that for the  $F' = 3$  transition, the two cyclic transitions  $|F = 2, m_F = 2\rangle \rightarrow |F' = 3, m'_F = 3\rangle$  and  $|F = 2, m_F = -2\rangle \rightarrow |F' = 3, m'_F = -3\rangle$  can be clearly separated. The clear detection signal at the untrapped transition  $|F = 2, m_F = -2\rangle \rightarrow |F' = 3, m'_F = -3\rangle$  demonstrates that the scattering process is much faster than the dynamics of atoms leaving the trap.

### 5.2. Atom cloud extension in the guide

The position of the magnetic guide above the chip surface can be aligned relative to the focus of the tapered lensed fiber at the detection region by adjusting the current  $I_g$  through the chip wire and the strength of the external magnetic field  $B_\perp$  perpendicular to the wire. The guide is located at height  $r_0 = (\mu_0/(2\pi)) \cdot I_g/B_\perp$ , where  $\mu_0$  is the vacuum permeability. Scanning the chip current at constant bias field, different slices through the guide potential can be probed, allowing us to examine the extension of the atomic cloud in the guide with only small changes to the potential shape, as shown in figure 7(a). Figure 7(b) shows the result of a scan shifting the guide potential minimum from 25 to 95  $\mu\text{m}$ . Maximum signal is retrieved if the guide minimum is aligned with the detection area, given by the 5  $\mu\text{m}$  focal spot of the tapered lensed fiber, and only the longitudinally fast atoms reach the outlying regions of the guide.

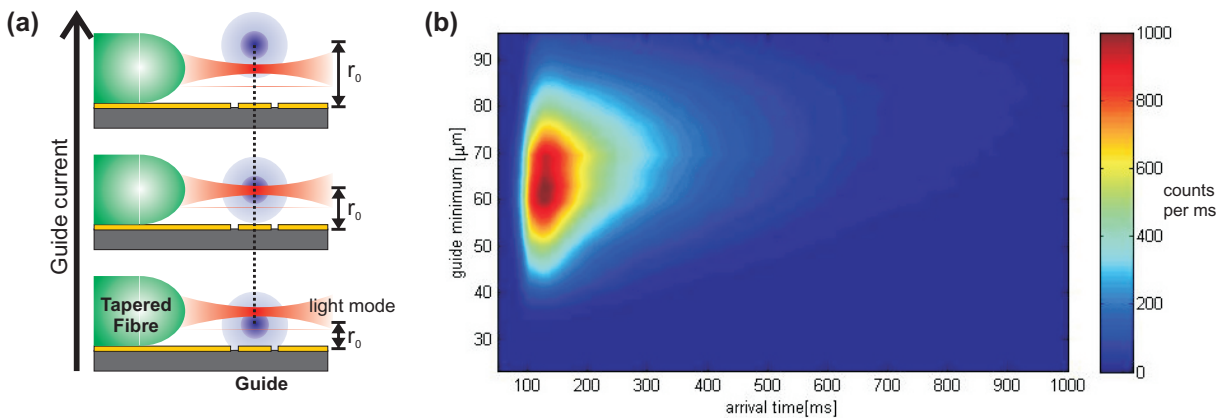


**Figure 7.** Probing the profile of atomic density in the guide. (a) Scanning the guide current allows probing the guide potential at different heights. A low guide current leads to the guide minimum being close to the chip, and atoms propagating higher in the guide are detected. (b) The scan reveals the transversal extension of the atoms in the guide potential. The optimal signal is achieved when the guide minimum is aligned with the tapered fiber focus at  $62.5 \mu\text{m}$ .

### 5.3. Time interval analysis (TIA)

TIA examines the temporal distance between neighboring events to draw conclusions on the statistical distribution of the atoms [64]. In contrast to the noise analysis presented in section 4.3, TIA does not require a series of measurements, but extracts statistical information from a single run of the experiment. Central to TIA is the probability  $p_0$  to measure no counts in a time bin of size  $t_b$ . For example: for independent counting events, such as multi-mode fluorescence from a constant source,  $p_0$  is a constant. The probability of finding a time interval of  $k$  bins *between two photon detection events* that contain no photon counts is given by  $P_{\text{TI}}(k) = (1 - p_0) p_0^k$ . It follows that  $\log P_{\text{TI}}(k)$  is a linear function of  $k$  for uncorrelated events.

The measured time interval distribution for atom detection events in our detector is shown in figure 8. It can be described by two superimposed exponential functions (red line, linear on the log scale of the graph). This suggests that we observe two distinct processes. An atom creates fluorescence counts according to its instantaneous fluorescence rate, while it is present in the interaction region. The fast decay of  $5.6 \pm 0.2 \mu\text{s}$  from figure 8 is a little bit faster than the  $7 \mu\text{s}$  estimated from the measurements of  $\alpha$  and the simple Monte Carlo model shown in figure 4. This is not very surprising, since the MC model is sensitive to an average rate for photon detection or an atom event, while the TIA is mostly sensitive to the instantaneous rate in the beginning, which will be faster. After a certain time [65] the atom leaves the detection region. Except for random background counts with very low probability, the detector sees no further light until the next atom arrives. Therefore, the steep slope for short time intervals is determined by the instantaneous fluorescence rate of individual atoms. For long time intervals, the slope is given by the atom arrival rate.

In the experiments presented here, we use thermal atoms in a multi-mode guide (typically  $> 10^3$  transverse modes are occupied); thus their statistical distribution can be well approximated by a Poisson distribution. Indeed, the linear relation between  $\log P_{\text{TI}}(k)$  and  $k$  for

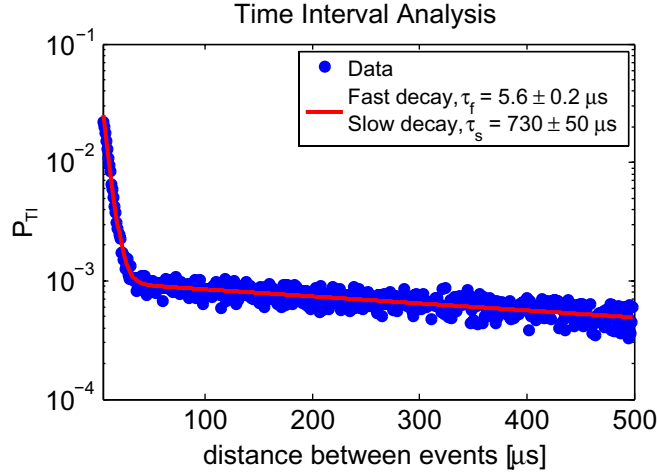


**Figure 8.** TIA: the data points show the probabilities for finding different time intervals  $t = k \cdot b$ , with bin size  $b = 1 \mu\text{s}$  and number of bins  $k$ , between successive photon detections in the low-density tail (arrival time 1800–1850 ms, see figure 3) of the atom distribution. The distribution is composed of two separate exponentials decaying on different timescales, as shown by a double exponential fit (red line). Short time intervals are dominated by the fluorescence burst of the atoms, hence the decay time  $\tau_f$  is related to the mean number of atoms present in the detection region. The long intervals are given by the atom arrival rate at the detector, hence the decay time  $\tau_s$  is the inverse of the atom arrival rate at the detector. The exponential fit demonstrates that the atoms arrive stochastically independently. Additionally, a Poissonian distribution of atom arrival times could be confirmed by comparing the slope of the measured distribution to the mean rate of atom detections.

times  $\gg \tau$  shows that the atoms arrive independently of each other. The observed slope in the TIA for long times is consistent with the measured atom rate, verifying a Poissonian distribution of arrival times in the multi-mode guide.

#### 5.4. Photon antibunching

A single atom can emit only one photon at any given time. Before a second photon can be emitted, the atom has to be transferred to the excited state again. Therefore, photon antibunching is expected to occur for single-atom detection events at timescales of the order of the excited state lifetime  $1/\Gamma = 26 \text{ ns}$  [66, 67]. The second-order intensity correlation function is given by

$$g^{(2)}(\delta t) = \frac{\langle \hat{E}^-(t) \hat{E}^-(t + \delta t) \hat{E}^+(t + \delta t) \hat{E}^+(t) \rangle}{\langle \hat{E}^-(t) \hat{E}^+(t) \rangle^2}. \quad (3)$$

Photon antibunching is characterized by  $g^{(2)}(\delta t) < 1$ , and for a single photon  $g^{(2)}(0) = 0$  is expected.

For late arrival times larger than 1000 ms, the atomic density in the guide is so low that collisional broadening and multi-atom effects can be completely neglected. In this regime, an

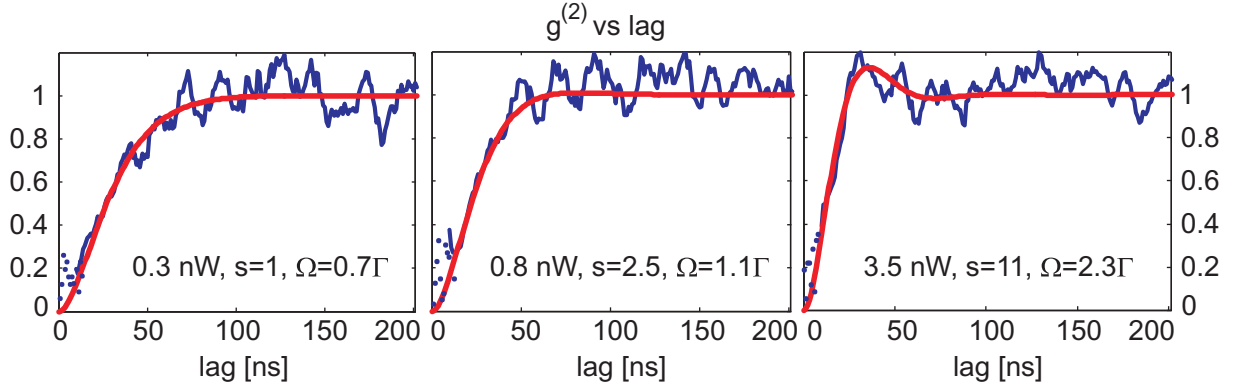


**Figure 9.** Photon antibunching: second-order intensity correlation function  $g^{(2)}(\delta t)$  for Rabi frequencies  $\Omega$  increasing from  $0.7\Gamma$  ( $s = I/I_{\text{sat}} = 1$ ) to  $2.3\Gamma$  ( $s = 11$ ). For a time lag shorter than the excited state lifetime of  $1/\Gamma = 26.2\text{ ns}$  the fluorescence exhibits photon antibunching. The blue curve shows the measured correlation function. The red line is a theoretical model (see equation (4)) for the corresponding Rabi frequency without free parameters. For small Rabi frequencies,  $g^{(2)}(\delta t)$  approaches the limiting value of 1 for large lags, while for  $\Omega = 2.3\Gamma$  a damped Rabi oscillation can be observed. Each graph is the result of 1000 single measurements.

approximation of  $g^{(2)}(\delta t)$  for arbitrary probe beam powers can be given if the illumination is on resonance [67]:

$$g^{(2)}(\delta t) = 1 - \left( \cos \zeta \delta t + \frac{3\Gamma}{2\zeta} \sin \zeta \delta t \right) e^{-3/2\Gamma \delta t}, \quad (4)$$

with  $\zeta = \sqrt{\Omega^2 - \Gamma^2/4}$  and  $\Omega$  denoting the Rabi frequency.

For high-efficiency atom detection, a single SPCM is employed, while correlation measurements require two SPCMs in Hanbury Brown–Twiss-like configuration. Consequently, for these measurements, the light from the collection fiber is sent on to a 50/50 beam splitter, and both output ports are coupled to separate SPCMs (see figure 2). The counts from the SPCM are recorded and time-stamped at 1 ns resolution by a multichannel counter card (FAST ComTec P7888 Multiscaler) in a dedicated computer. Special care has to be taken to compensate for secondary emission effects in the SPCMs.

Figure 9(a) shows three different measurements of  $g^{(2)}(\delta t)$  from the cross-correlation of photon counts in two SPCMs in a Hanbury Brown–Twiss-type setup for Rabi frequencies ranging from  $0.7\Gamma$  to  $2.3\Gamma$ . The correlation function was reconstructed from the low-density tail of the atom distribution where the mean atomic distance is large enough to guarantee the presence of at most one atom in the detection region at any given time. We find beautiful agreement between the measurements and the theoretical (parameter-free) prediction according to equation (4). For  $\Omega = 2.3\Gamma$ , the onset of Rabi oscillations in the correlation function can be observed.

We extract a value of  $g^{(2)}(0) = 0.05$  from 4400 single measurements at  $\Omega = 1.3\Gamma$ . The mean photon count rate for each single measurement was approximately 3500 cps. If coincidental background correlations are corrected for, the correlation reduces to a value

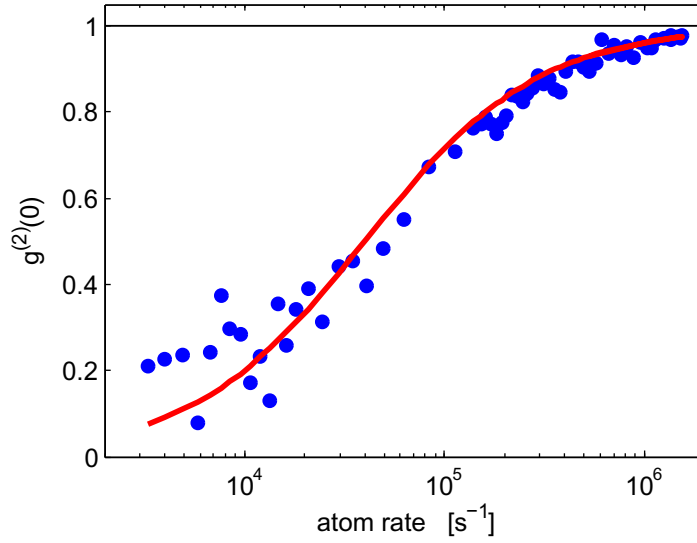


**Figure 10.** Photon antibunching  $g^{(2)}(0)$  as a function of the atom arrival rate over three orders of magnitude. The red line is the theoretical limit given by equation (6).

compatible with zero ( $g^{(2)}(0) = 0.005 \pm 0.010$ ), demonstrating that we are able to observe near-perfect photon antibunching in the emission of single atoms passing the detector. This is clear proof that our detector is capable of detecting single atoms in passage.

Our detector allows us to examine photon antibunching as a function of the atom density by evaluating  $g^{(2)}(0)$  as a function of the arrival time, as the atom pulse passes the detector (compare the signal shape in figure 3(a)). For a single-mode field with mean photon number  $\langle n \rangle$ , the second-order correlation at lag 0 is limited by [67]

$$g^{(2)}(0) \geq 1 - \frac{1}{\langle n \rangle}, \quad \forall \langle n \rangle \geq 1, \quad (5)$$

while for  $\langle n \rangle < 1$  the lower limit is 0. For a Fock state with fixed photon number  $n$ , inequality (5) becomes an equality and the minimal value of  $g^{(2)}(0)$  is reached. While for classical light sources  $1 \leq g^{(2)}(0) \leq \infty$  holds, the region  $g^{(2)}(0) < 1$  is exclusively non-classical and can only be reached by quantum emitters.

Since  $g^{(2)}(\delta t)$  is evaluated when at least one photon count has been recorded, the mean photon number  $\langle n \rangle$  has to be calculated under the condition  $n \geq 1$ . This leads to  $\langle n \rangle = \alpha \langle m \rangle / (1 - \exp(-\alpha \langle m \rangle))$ , with mean emitter number  $\langle m \rangle$ . Hence,  $g^{(2)}(0)$  is limited by

$$g^{(2)}(0) \geq 1 - \frac{1 - \exp(-\alpha \langle m \rangle)}{\alpha \langle m \rangle}. \quad (6)$$

As can be seen from figure 10, the measured  $g^{(2)}(0)$  follows the expected shape for the full atom pulse duration. With this measurement, we extend the original experimental investigation [66, 68] of the influence of atomic density on the second-order correlation function over almost three orders of magnitude change in atomic density.

**Table 3.** Single-atom detection efficiency as a function of the integration time for an improved system using a commercially available fiber with  $NA = 0.53$  ( $\eta_{ph} = 3.8\%$ ). Numbers in parentheses denote the corresponding values for two detection fibers of  $NA = 0.53$  ( $\eta_{ph} = 7.6\%$ ). The false detection probability  $p_f$  and the SNR are given for the present background rate of 310 cps and the improved rate of 55 cps for low dark count photon counting modules.

$t_{int}$	$\alpha$ (cpa)	$\eta_{at}$	$p_f$	SNR
$300 \mu s$	4.5 (9.0)	99% (> 99.99%)	< 4.3% (< 7.6%)	273 (545)
$45 \mu s$	3.8 (7.6)	98% (> 99.9%)	< 0.7% (< 1.2%)	230 (460)
$20 \mu s$	3.0 (6.0)	95% (> 99.7%)	< 0.3% (< 0.5%)	182 (364)

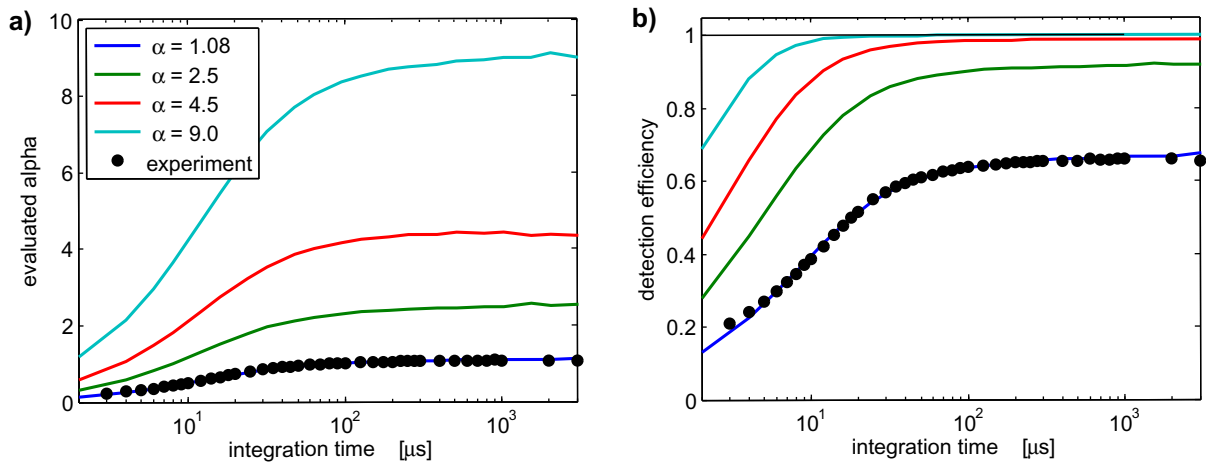


**Figure 11.** Projected performance of the detector when light collection is improved to yield  $\alpha = 2.5, 4.5$  or  $9.0$  cpa, respectively. The curves are calculated according to the Monte Carlo model discussed in section 4.3. The performance of the present detector with  $\alpha = 1.08$  is shown for comparison. (a)  $\alpha$  versus integration time. (b) Projected detection efficiency.

## 6. Future improvements

The detection efficiency  $\eta_{at} = 66\%$  of the current detector setup is mainly limited by the photon collection efficiency  $\eta_{coll} = 1.9\%$  given by the numerical aperture  $NA=0.275$  of the multi-mode collection fiber. The detection efficiency can be significantly improved by increasing  $\eta_{coll}$ .

A single-atom detection efficiency close to unity can be achieved by substituting the present detection fiber ( $NA = 0.275$ ) with a fiber with  $NA = 0.53$ . This increases the photon collection efficiency to  $\eta_{coll} = 7.6\%$ , which would result in  $\alpha = 4.5$  cpa (see table 3 and figure 11). Such an improved system is expected to reach a single-atom detection efficiency of 95%, even at 50 kHz bandwidth.

The detection efficiency can be further improved by collecting light from two sides by mounting two facing high-NA detection fibers. Using two  $NA = 0.53$  fibers, one can reach  $\eta_{at} > 99\%$  at integration times below  $t_{int} = 20 \mu s$ . For such a detector system, a signal strength of  $\alpha = 9$  cpa is expected.

With either improvement implemented, high-fidelity atom counting (in the sense of identifying the number of simultaneously present atoms) and observation of atom transits in transient count rate analysis will become feasible.

## 7. Conclusion

To conclude, we have built and evaluated an optical fiber-based atom detector that is fully integrated on an atom chip, alignment-free by fabrication, mechanically very robust and capable of detecting single  $^{87}\text{Rb}$  atoms by counting fluorescence photons. The detector allows us to selectively detect the  $F = 2$  and  $F = 1$  hyperfine states of  $^{87}\text{Rb}$  at efficiencies of  $\eta_{\text{at}} = 66$  and  $64\%$ , respectively. It enables spatially and spectrally highly selective probing, while at the same time offering extremely robust operation. The total background is dominated by the dark count rate of the employed SPCMs. High-efficiency detection is possible, as well as low-noise, high-bandwidth detection. At  $20 \mu\text{s}$  integration time, single-atom detection can be performed at an efficiency of  $\eta_{\text{at}} = 50\%$  and  $\text{SNR} > 100$ . The disadvantage of fluorescence detection is the destructive nature of the process, which our detector shares with photon detection. Our detector can therefore be best characterized as the atom optic equivalent of an avalanche PD-type SPCM.

Low noise, high efficiency and insensitivity to stray light are achieved using fiber optics to create very selective excitation of the atoms in a small, matched observation volume.

The detection efficiency is currently limited by the NA of the multimode collection fiber. A straightforward substitution of the employed  $\text{NA} = 0.275$  fiber by a commercially available fiber with  $\text{NA} = 0.53$  increases the photon collection to  $\alpha = 4.5$  cpa and the single-atom detection efficiency to  $95\%$  at  $50 \text{ kHz}$  bandwidth. Employing two collection fibers,  $\alpha = 9$  cpa and  $\eta_{\text{at}} > 99\%$  at integration times below  $t_{\text{int}} = 20 \mu\text{s}$  can be achieved. With these improvements, full atom counting becomes feasible.

The high efficiency, SNR and bandwidth of our integrated detector make it suitable for many physical systems where only a few photons can be scattered. A prime example would be detecting trapped cold molecules. With its extremely low sensitivity to stray light, our detector is well suited for studies of correlated atomic systems and scalable quantum experiments on a single-atom or -molecule level.

## Acknowledgments

We thank A Haase and M Schwarz for help in the early stages of the experiment and K-H Brenner and I Bar-Joseph for help in the fabrication. We gratefully acknowledge financial support from the Landesstiftung Baden-Württemberg, the European Union (HIP), the Austrian Nano-initiative (PLATON-NAP) and the FWF. The atom chip shown in this work was fabricated at The Braun Submicron Center at Weizmann Institute of Science, Rehovot, IL.

## References

- [1] Hurst G S, Nayfeh M H and Young J P 1977 *Appl. Phys. Lett.* **30** 229–31
- [2] Öttl A, Ritter St, Köhl M and Esslinger T 2005 *Phys. Rev. Lett.* **95** 090404
- [3] Aoki T, Dayan B, Wilcut E, Bowen W P, Parkins A S, Kippenberg T J, Vahala K J and Kimble H J 2006 *Nature* **443** 671–4
- [4] Hood C J, Lynn T W, Doherty A C, Parkins A S and Kimble H J 2000 *Science* **287** 1447–53

- [5] Münstermann P, Fischer T, Maunz P, Pinkse P W H and Rempe G 1999 *Phys. Rev. Lett.* **82** 3791–4
- [6] Mabuchi H, Turchette Q A, Chapman M S and Kimble H J 1996 *Opt. Lett.* **21** 1393
- [7] Mabuchi H, Ye J and Kimble H J 1999 *Appl. Phys. B* **68** 1095
- [8] Haase A, Hessmo B and Schmiedmayer J 2006 *Opt. Lett.* **31** 268–70
- [9] Teper I, Lin Y J and Vuletić V 2006 *Phys. Rev. Lett.* **97** 023002
- [10] Trupke M, Goldwin J, Darquié B, Dutier G, Eriksson S, Ashmore J and Hinds E A 2007 *Phys. Rev. Lett.* **99** 063601
- [11] Colombe Y, Steinmetz T, Dubois G, Linke F, Hunger D and Reichel J 2007 *Nature* **450** 272–6
- [12] Terraciano M L, Olson Knell R, Norris D G, Jing J, Fernandez A and Orozco L A 2009 *Nat. Phys.* **5** 480–4
- [13] Neuhauser W, Hohenstatt M, Toschek P E and Dehmelt H G 1980 *Phys. Rev. A* **22** 1137
- [14] Wineland D J and Itano W M 1981 *Phys. Lett. A* **82** 75
- [15] Diedrich F and Walther H 1987 *Phys. Rev. Lett.* **58** 203–6
- [16] Leibfried D, Blatt R, Monroe C and Wineland D 2003 *Rev. Mod. Phys.* **75** 281–324
- [17] Myerson A H, Szwer D J, Webster S C, Allcock D T C, Curtis M J, Imreh G, Sherman J A, Stacey D N, Steane A M and Lucas D M 2008 *Phys. Rev. Lett.* **100** 200502
- [18] Hu Z and Kimble H J 1994 *Opt. Lett.* **19** 1888–90
- [19] Ruschewitz F, Bettermann D, Peng J L and Ertmer W 1996 *Europhys. Lett.* **34** 651–6
- [20] Haubrich D, Schadwinkel H, Strauch F, Ueberholz B, Wynands R and Meschede D 1996 *Europhys. Lett.* **34** 663–8
- [21] Willems P A, Boyd R A, Bliss J L and Libbrecht K G 1997 *Phys. Rev. Lett.* **78** 1660–3
- [22] Frese D, Ueberholz B, Kuhr S, Alt W, Schrader D, Gomer V and Meschede D 2000 *Phys. Rev. Lett.* **85** 3777–80
- [23] Kuhr S, Alt W, Schrader D, Mueller M, Gomer V and Meschede D 2001 *Science* **293** 278–80
- [24] Schlosser N, Raymond G, Protsenko I and Grangier P 2001 *Nature* **411** 1024–7
- [25] Miroshnychenko Y, Schrader D, Kuhr S, Alt W, Dotsenko I, Khudaverdyan M, Rauschenbeutel A and Meschede D 2003 *Opt. Express* **11** 3498
- [26] Darquié B, Jones M P A, Dingjan J, Beugnon J, Bergamini S, Sortais Y, Messin G, Browaeys A and Grangier P 2005 *Science* **309** 454–6
- [27] Miroshnychenko Y, Alt W, Dotsenko I, Förster L, Khudaverdyan M, Meschede D, Schrader D and Rauschenbeutel A 2006 *Nature* **442** 151
- [28] Nelson K D, Li X and Weiss D S 2007 *Nat. Phys.* **3** 556
- [29] Karski M, Foerster L, Choi J M, Alt W, Widera A and Meschede D 2009 *Phys. Rev. Lett.* **201** 053001
- [30] Bakr W S, Gillen J I, Peng A, Fölling S and Greiner M 2009 *Nature* **462** 74–7
- [31] Esslinger T, Hemmerich A and Hänsch T W 1992 *Opt. Commun.* **93** 49–53
- [32] Bondo T, Hennrich M, Legero T, Rempe G and Kuhn A 2006 *Opt. Commun.* **264** 271–7
- [33] Bücker R, Perrin A, Manz S, Betz T, Koller Ch, Plisson T, Rottmann J, Schumm T and Schmiedmayer J 2009 *New J. Phys.* **11** 103039
- [34] Folman R, Krüger P, Cassettari D, Hessmo B, Maier T and Schmiedmayer J 2000 *Phys. Rev. Lett.* **84** 4749
- [35] Folman R, Krüger P, Schmiedmayer J, Denschlag J and Henkel C 2002 *Adv. At. Mol. Opt. Phys.* **48** 263–356
- [36] Reichel J 2002 *Appl. Phys. B* **75** 469–87
- [37] Fortagh J and Zimmermann C 2007 *Rev. Mod. Phys.* **79** 235
- [38] Krüger P, Luo X, Klein M W, Brugger K, Haase A, Wildermuth S, Groth S, Bar-Joseph I, Folman R and Schmiedmayer J 2003 *Phys. Rev. Lett.* **91** 233201
- [39] Hänsel W, Reichel J, Hommelhoff P and Hänsch T W 2001 *Phys. Rev. Lett.* **86** 608
- [40] Cassettari D, Hessmo B, Folman R, Maier T and Schmiedmayer J 2000 *Phys. Rev. Lett.* **85** 5483  
Cassettari D *et al* 2000 *Appl. Phys. B* **70** 721
- [41] Ott H, Fortagh J, Schlotterbeck G, Grossmann A and Zimmermann C 2001 *Phys. Rev. Lett.* **87** 230401
- [42] Hänsel W, Hommelhoff P, Hänsch T W and Reichel J 2001 *Nature* **413** 498

- [43] Schneider S, Kasper A, vom Hagen Ch, Bartenstein M, Engeser B, Schumm T, Bar-Joseph I, Folman R, Feenstra L and Schmiedmayer J 2003 *Phys. Rev. A* **69** 023612
- [44] Schumm T, Hofferberth S, Andersson L M, Wildermuth S, Groth S, Bar-Joseph I, Schmiedmayer J and Krüger P 2005 *Nat. Phys.* **1** 57
- [45] Bohi P, Riedel M F, Hoffrogge J, Reichel J, Hänsch T W and Treutlein P 2009 *Nat. Phys.* **5** 592–7
- [46] Gallego D, Hofferberth S, Schumm T, Krüger P and Schmiedmayer J 2009 *Opt. Lett.* **34** 3463–5
- [47] Denschlag J, Cassettari D, Chenet A, Schneider S and Schmiedmayer J 1999 *Appl. Phys. B* **69** 291–301
- [48] Grüner B, Jag M, Stibor A, Visanescu G, Häffner M, Kern D, Günther A and Fortágh J 2009 *Phys. Rev. A* **80** 063422
- [49] Günther A, Bender H, Stibor A, Fortágh J and Zimmermann C 2009 *Phys. Rev. A* **80** 011604
- [50] Quinto-Su P, Tschernock M, Holmes M and Bigelow N 2004 *Opt. Express* **12** 5098–103
- [51] Wilzbach M, Heine D, Groth S, Liu X, Raub T, Hessmo B and Schmiedmayer J 2009 *Opt. Lett.* **34** 259–61
- [52] Petrov P G, Nyman R A, Trupke M, Hinds E A, Kohnen M and Succo M 2009 arXiv:0912.4460v1
- [53] Horak P, Klappauf B G, Haase A, Folman R, Schmiedmayer J, Domokos P and Hinds E A 2003 *Phys. Rev. A* **67** 043806
- [54] Groth S, Krüger P, Wildermuth S, Folman R, Fernholz T, Schmiedmayer J, Mahalu D and Bar-Joseph I 2004 *Appl. Phys. Lett.* **85** 2980
- [55] Trinker M, Groth S, Haslinger S, Manz S, Betz T, Schneider S, Bar-Joseph I, Schumm T and Schmiedmayer J 2008 *Appl. Phys. Lett.* **92** 254102
- [56] Liu X, Brenner K-H, Wilzbach M, Schwarz M, Fernholz T and Schmiedmayer J 2005 *Appl. Opt.* **44** 6857–60
- [57] Heine D, Wilzbach M, Raub T, Hessmo B and Schmiedmayer J 2009 *Phys. Rev. A* **79** 021804
- [58] del Campo A and Greiner C 2007 *J. Micromech. Microeng.* **17** R81–95
- [59] Wilzbach M *et al* 2006 *Fortschr. Phys.* **54** 746–64
- [60] Abraham E R I and Cornell E A 1998 *Appl. Opt.* **37** 1762–3
- [61] Wildermuth S, Krüger P, Becker C, Brajdic M, Haupt S, Kasper A, Folman R and Schmiedmayer J 2004 *Phys. Rev. A* **69** 030901
- [62] Rohringer W, Bücken R, Manz S, Betz T, Koller Ch, Goebel M, Perrin A, Schmiedmayer J and Schumm T 2008 *Appl. Phys. Lett.* **93** 264101
- [63] Mandel L and Wolf E 1965 *Rev. Mod. Phys.* **37** 231–87
- [64] Köhl M, Öttl A, Ritter S, Donner T, Bourdel T and Esslinger T 2007 *Appl. Phys. B* **86** 391–3
- [65] Heine D 2008 *PhD Thesis* Universität Heidelberg
- [66] Kimble H J, Dagenais M and Mandel L 1977 *Phys. Rev. Lett.* **39** 691–5
- [67] Loudon R 2000 *The Quantum Theory of Light* 3rd edn (Oxford: Oxford Science)
- [68] Kimble H J, Dagenais M and Mandel L 1978 *Phys. Rev. A* **18** 201–7